

---

# S<sup>2</sup>OMGAN: Shortcut from Remote Sensing Images to Online Maps

---

**Xu Chen, Songqiang Chen, Tian Xu, Bangguo Yin**  
School of Computer Science, Wuhan University  
{xuchen, imcsq, xutian, ybg}@whu.edu.cn

**Jian Peng, Xiaoming Mei, Haifeng Li\***  
School of Geosciences and Info-Physics, Central South University  
lihaifeng@csu.edu.cn

## Abstract

Traditional online maps, widely used on Internet such as Google map and Baidu map, are rendered from vector data. Timely updating online maps from vector data, of which the generating is time-consuming, is a difficult mission. It is a shortcut to generate online maps in time from remote sensing images, which can be acquired timely without vector data. However, this mission used to be challenging or even impossible. Inspired by image-to-image translation (img2img) techniques based on generative adversarial network (GAN), we propose a semi-supervised structure-augmented online map GAN (S<sup>2</sup>OMGAN) model to generate online maps directly from remote sensing images. In this model, we designed a semi-supervised learning strategy to pre-train S<sup>2</sup>OMGAN on rich unpaired samples and finetune it on limited paired samples in reality. We also designed image gradient L1 loss and image gradient structure loss to generate an online map with global topological relationship and detailed edge curves of objects, which are important in cartography. Moreover, we propose edge structural similarity index (ESSI) as a metric to evaluate the quality of topological consistency between generated online maps and ground truths. Experimental results present that S<sup>2</sup>OMGAN outperforms state-of-the-art (SOTA) works according to mean squared error, structural similarity index and ESSI. Also, S<sup>2</sup>OMGAN wins more approval than SOTA in the human perceptual test on visual realism of cartography. Our work shows that S<sup>2</sup>OMGAN is potentially a new paradigm to produce online maps. Our implementation of the S<sup>2</sup>OMGAN is available at <https://github.com/imcsq/S2OMGAN>.

## 1 Introduction

Online maps service is widely used in several fields and the demand for in-time online maps is increasing dramatically. Traditional manual cartography relies on the vectorization of map and is time consuming[1], which makes the timely update of object features on maps difficult. However, remote sensing images can be acquired in time. Thus, generating online maps directly from remote sensing images without the vector data is one way to reduce the time cost.

Though used to be thought of as a challenge or even an impossible mission[2], the recent rise of the image-to-image translation (img2img) techniques based on generative adversarial network (GAN) offers a method for the map generation directly from remote sensing images because it can be viewed as an img2img task.

In recent years, GAN and img2img techniques are used to produce images for various purposes, such as supersolution[3–5], image classification[6–8], dataset augmentation[9–11], and specific domain image generation[12–15].

Img2img technique and its application developed quickly. First, Pix2Pix[16] and CycleGAN[17]

---

\*Corresponding author: lihaifeng@csu.edu.cn

were put forward as two typical img2img techniques. Then, [18] and [19] tried to improve generating quality by adding a shared latent space and an attention layer to CycleGAN[17], respectively. These img2img models were applied to generate multistyle maps from simple-styled maps that derived from vector data [2] and online maps from remote sensing images [20]. However, these generated maps suffered erroneous topological relations and blurred details. The current flaws of applying general img2img to map generation from remote sensing images lay in three aspects.

First, the lack of paired samples, which consist of a remote sensing image and its corresponding online map, makes the results not good enough. For example, the latest remote sensing images may lack corresponding online maps while online maps may be generated from other methods without corresponding remote sensing images. However, unpaired data could increase the diversity of object features to improve the generalization ability of the model.

Second, though several studies reduced the pixel-wise L1 distance between output and ground truths to improve the models [12, 16, 17, 21], these studies ignored the topological relationship among pixels, which is vital in cartography [22].

Third, the metric to evaluate quality of generated online map is lacked. A few metrics are proposed to evaluate the realism of the images generated by GAN [23], [24], but a high quality map should not only be of high realism but also be able to replicate correct features in ground truth. Instead, full-reference metrics provide a pixel-wise comparison between the generated image and the ground truth, but no metrics focus on topological relationship of objects.

In the current work, we designed a semi-supervised learning strategy to fit the model to paired and unpaired samples. Our main ideas and contributions are listed as follows:

(1) We proposed a novel online maps generating model named S<sup>2</sup>OMGAN, which introduced a semi-supervised learning strategy to train the model on massive unpaired samples and a small amount of paired samples.

(2) We designed image gradient L1 loss and image gradient structure to transform the topological relationship among objects on maps to the topological relationship among edge curves of objects. They encouraged S<sup>2</sup>OMGAN to generate maps of better details and topological relationship than baselines.

(3) We proposed a full-reference image quality metric, edge structural similarity index (ESSI), to measure the topological consistency between the generated and the real maps by the correlation between random variables, to which the edge images of the generated and the real maps are transformed.

(4) We compared S<sup>2</sup>OMGAN with SOTA baselines under mean square error (MSE), structural similarity index (SSIM), ESSI, and human perception test. The results show that S<sup>2</sup>OMGAN outperforms SOTA on online maps generating tasks.

This paper is structured as follows. In Section 2, related works are represented. In Section 3, the S<sup>2</sup>OMGAN framework and its losses are discussed in detail. Specifically, the two proposed gradient losses are introduced. The experiment and results are discussed in Section 4. Finally, the advantages and shortcomings of our model as well as our future work are mentioned in Section 5.

## 2 Related Work

We divided the current related work into four aspects. Previous studies proposed several basic img2img translation methods. Then, other studies modified the basic model to obtain good images but still for general usage. Recently, studies tried to occupy img2img methods to generate maps. Besides, evaluating GAN is a hot topic that inspires other research.

### 2.1 Image to Image Translation

Pix2Pix [16] is a typical case of this work that adopts a conditional GAN (cGAN) [25] to learn the translation in a supervised way. In the Pix2Pix model, a generator network is trained to produce valid and realistic images in the target domain corresponding to the input images in the source domain. This process is constrained by an adversarial and an L1 loss, which are considered as a sufficient high- and low-frequency structure restriction, respectively. However, Pix2Pix must be trained on paired samples due to its supervised loss. To address these constraints, [17] proposed CycleGAN by imposing cycle-consistency, which was built on the fact that an image

should be reconstructed correctly after translating twice. This premise allows img2img models to be trained using unpaired datasets. However, the lack of ground truths makes the method less robust than a supervised one. These classical img2img translating models are the bases of our method.

## 2.2 Augmented Image to Image Translating

After the two classic types of img2img models proposed, recent works tried to improve the results of the models for a universal or specific purpose. [18, 26–30] focused on the impact of latent features and modified the architecture of the proposed model to make improved, multiple, or other amazing results. Others like [19, 31–34] advocated supplementing helpful components to improve image generation, such as adding an attention layer into the model. In our work, we combined an important component with the structure of proposed models to improve performance on online map generation.

## 2.3 Latest Try on Using img2img technique to Generate Online Maps

With the popularity of img2img, studies tried applying this method to generate online maps. [2] used Pix2Pix and CycleGAN to transfer online maps from simple-styled maps generated based on vectorized data. [20] put forward a model with style and content losses, based on cGAN to generate online maps from satellite images. Both works verified the basic feasibility of the task and left a few quality-related problems, such as incorrect topological relations of objects.

## 2.4 Metrics of Img2Img Translation Work

Metrics, such as inception score (IS) [23] and Frechet inception distance (FID) [24], were proposed to evaluate the quality of images generated by GAN. However, IS and FID are not suitable for map translation task. These metrics are generally used to measure an image-generative model based on the distance of probability distribution between ground truths and generated images. The distance of probability cannot measure the quality of one single generated map compared to its ground truth because map translation demands that a generated map can replicate the details of a real map. In geoscience, [35] proposed a quality assessment for classification and cluster maps, which compared labeling and segmentation among cluster maps. However, this method cannot measure the accuracy of generated online maps. Instead, full-reference image quality assessment indexes, such as MSE [36] and SSIM [37], are suitable for assessing map translation tasks. MSE measures global average L2 distance of pixels between two images but cannot measure the pixel-wise structure. In contrast to MSE, SSIM considers pixel-wise structure, which can evaluate structural replication of generated maps. [38] and [39] further investigated the significance of the first-order derivative of pixels of images as well as the gradient of images to image quality assessment. This method inspired our work on generated map quality assessment.

# 3 Methods

## 3.1 S<sup>2</sup>OMGAN Framework

The S<sup>2</sup>OMGAN model includes two GANs to generate online maps from input remote sensing images ( $G_{R \rightarrow M}$ ,  $D_M$ ) (where  $G_{R \rightarrow M}$  is the generator producing maps from the remote sensing images, and  $D_M$  is the discriminator to discriminate against the generated maps) and generate remote sensing images from online maps ( $G_{M \rightarrow R}$ ,  $D_R$ ) (where  $G_{M \rightarrow R}$  is the generator producing the remote sensing images from the maps, and  $D_R$  is the discriminator to discriminate against the generated remote sensing images). As shown in Figure 1, S<sup>2</sup>OMGAN achieves semi-supervised learning by combining a supervised and an unsupervised learning strategies, which will be discussed in Section 3.2. Moreover, S<sup>2</sup>OMGAN focuses not only on the correct value of each pixel in the generated maps but also on the quality of topological relationship in the output, which will be discussed in detail in Section 3.3.

The architecture of the S<sup>2</sup>OMGAN is shown in Figure 1(A). A remote sensing image is sent to the

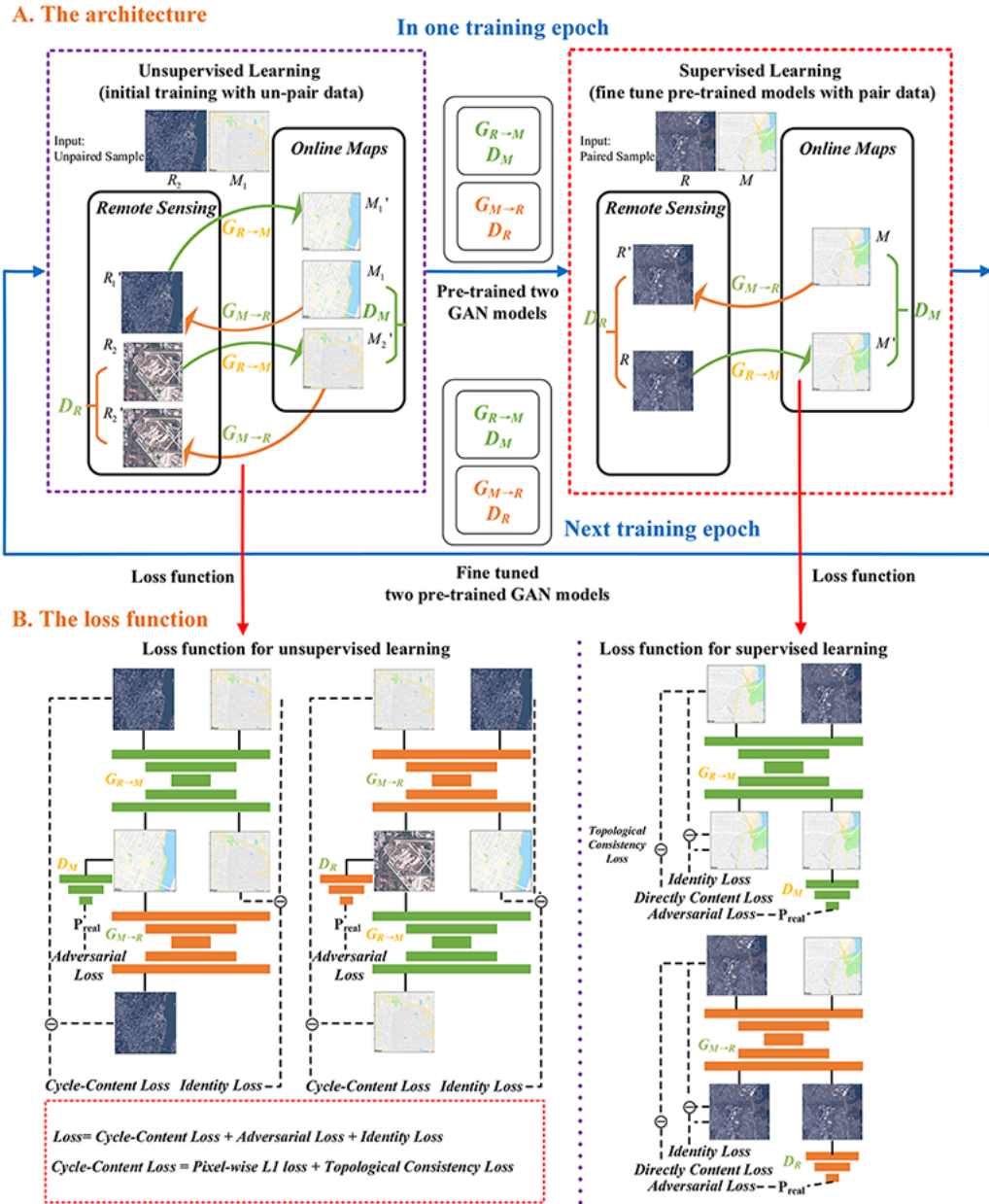


Figure 1: A S<sup>2</sup>OMGAN Method Overview; B Unsupervised learning process and supervised learning process in detail.

generator of online maps generating GAN to generate corresponding online maps. The other three networks only work during the training process to help model learning. During the training period, in every epoch, we first trained the model on unpaired samples with unsupervised learning to train initially the weight of 2 GANs (4 networks). we trained the model with two "Remote Sensing Image - Online Maps Cycle Consistency (RSI-OM-CyC)" (discussed in Section 3.2) in an unsupervised way due to lack of the corresponding map of the unpaired remote sensing images and corresponding remote sensing images of the unpaired map. The model is then trained on paired samples with supervised learning for fine-tuning. When training on paired data, the ground truth of a remote sensing image is its corresponding online map and vice versa. Thus, we trained the model in a semi-supervised way.

### 3.2 Loss Function in Semi-supervised Learning

Given the existence of various types of objects in map and not as many paired samples available all the time, as described in Section 1, we needed to learn to translate available paired and unpaired samples. Therefore, we designed a semi-supervised learning strategy that combined unsupervised and supervised learning, as Figure 1(A) shows. This allowed us to train our model on paired and unpaired training samples.

As an img2img translation work, we constrained the model learning with three classic types of loss, namely, content loss, adversarial loss, and identity loss, as previous works did [16, 17].

$$\mathcal{L} = \lambda_{ctn} \mathcal{L}_{ctn} + \lambda_{adv} \mathcal{L}_{adv} + \lambda_{idt} \mathcal{L}_{idt} \quad (1)$$

#### 3.2.1 Content Loss

Content loss is introduced as a condition in img2img translation GAN to evaluate directly how similar is a generated image to a real image. The loss consist of the pixel-wise L1 distance, image gradient L1, and image gradient structure losses. These losses would be selected in different stages.

We designed two types of content losses suitable to the unsupervised and supervised learning process equation 2 as shown in Figure 1(B).

$$\mathcal{L}_{ctn} = \mathcal{L}_{ctn}^{R \rightarrow M \rightarrow R} + \mathcal{L}_{ctn}^{M \rightarrow R \rightarrow M} + \mathcal{L}_{ctn}^{M \rightarrow R} + \mathcal{L}_{ctn}^{R \rightarrow M} \quad (2)$$

where  $\mathcal{L}_{ctn}^{R \rightarrow M \rightarrow R}$  and  $\mathcal{L}_{ctn}^{M \rightarrow R \rightarrow M}$  are the RSI-OM-CyC losses, while  $\mathcal{L}_{ctn}^{M \rightarrow R}$  and  $\mathcal{L}_{ctn}^{R \rightarrow M}$  are the Direct-Content losses.

**RSI-OM-CyC Loss:** When training on unpaired samples, the corresponding map is lacked when processing an unpaired remote sensing image and similar to that of an unpaired map. To compare pixel values between the generated and the real images in this process, we employed cycle-consistency [17] to build an unsupervised learning strategy. Cycle-consistency demands that the image translation cycle should bring the input image back to the original image. The two "Remote Sensing Image - Online Maps Cycle Consistency (RSI-OM-CyC)" are in our task. Specifically, for each remote sensing image  $x_R$ , the following  $x_R \rightarrow G_{R \rightarrow M}(x_R) \rightarrow G_{M \rightarrow R}(G_{R \rightarrow M}(x_R)) \approx x_R$  should be presented as the RMR-Cycle. For each online map  $x_M$ , the following  $x_M \rightarrow G_{M \rightarrow R}(x_M) \rightarrow G_{R \rightarrow M}(G_{M \rightarrow R}(x_M)) \approx x_M$  should be presented as the MRM-Cycle. For the RMR-Cycle, only the pixel-wise L1 loss ( $\mathcal{L}_{L1}$ ) is employed to guide the model to improve cycle-consistency through decreasing the mean difference of pixel value between a generated and its corresponding real remote sensing image equation 3. By contrast, for MRM-Cycle, the cycle-content loss is complicated. Besides the pixel-wise L1 loss, the image gradient L1 loss (GraL1 loss,  $\mathcal{L}_{gral1}$ ) and the image gradient structure loss (GraStr loss,  $\mathcal{L}_{grastr}$ ) are employed equation 4 to guide the model to improve cycle-consistency through improving topological consistency, which would be discussed in detail in Section 3.3

$$\mathcal{L}_{ctn}^{R \rightarrow M \rightarrow R} = \lambda_{L1u} \mathcal{L}_{L1} = \lambda_{L1u} \mathbb{E}_{x_R \sim p} [\|G_{M \rightarrow R}(G_{R \rightarrow M}(x_R)) - x_R\|_1] \quad (3)$$

$$\begin{aligned}
\mathcal{L}_{ctn}^{M \rightarrow R \rightarrow M} &= \lambda_{L1u} \mathcal{L}_{L1} + \mathcal{L}_{gral1} + \mathcal{L}_{grastr} \\
&= \lambda_{L1u} \mathbb{E}_{x_M \sim p} [\|G_{R \rightarrow M}(G_{M \rightarrow R}(x_M)) - x_M\|_1] \\
&\quad + \mathbb{E}_{x_M \sim p} [\|\mathcal{G}(G_{R \rightarrow M}(G_{M \rightarrow R}(x_M))) - \mathcal{G}(x_M)\|_1] \\
&\quad + \mathbb{E}_{x_M \sim p} [2 \\
&\quad - \frac{1}{N-1} \sum_{j=0}^{N-2} \frac{|\sigma_{\mathcal{G}_j(x_M)} \mathcal{G}_j(G_{R \rightarrow M}(G_{M \rightarrow R}(x_M)))| + C_1}{|\sigma_{\mathcal{G}_j(x_M)} \sigma_{\mathcal{G}_j(G_{R \rightarrow M}(G_{M \rightarrow R}(x_M)))}| + C_1} \\
&\quad - \frac{1}{M-1} \sum_{i=0}^{M-2} \frac{|\sigma_{\mathcal{G}_i(x_M)} \mathcal{G}_i(G_{R \rightarrow M}(G_{M \rightarrow R}(x_M)))| + C_2}{|\sigma_{\mathcal{G}_i(x_M)} \sigma_{\mathcal{G}_i(G_{R \rightarrow M}(G_{M \rightarrow R}(x_M)))}| + C_2}]
\end{aligned} \tag{4}$$

where  $\lambda$  is a coefficient for fine-tuning;  $\mathcal{L}_{L1}$  is the pixel-wise L1 loss;  $\mathcal{L}_{gral1}$  is the image gradient L1 loss; and  $\mathcal{L}_{grastr}$  is the image gradient structure loss.

**Direct-Content Loss:** Direct-Content Loss is introduced to generate remote sensing image with the ground truth for training on paired samples. Direct-Content Loss has two forms for different process. For the process of the generation from an online map to a remote sensing image, only the pixel-wise L1 loss is employed to measure the mean difference of pixels between a generated remote sensing image and its ground truth equation 5. For the process of the generation from a remote sensing image to an online map, the GraL1 loss and the GraStr loss are employed to measure the topological consistency between the generated map and the ground truth besides the pixel-wise L1 loss equation 6.

$$\mathcal{L}_{ctn}^{M \rightarrow R} = \lambda_{L1} \mathcal{L}_{L1} = \lambda_{L1} \mathbb{E}_{x_M \sim p} [\|G_{M \rightarrow R}(x_M) - x_R\|_1] \tag{5}$$

$$\begin{aligned}
\mathcal{L}_{ctn}^{R \rightarrow M} &= \lambda_{L1} \mathcal{L}_{L1} + \mathcal{L}_{gral1} + \mathcal{L}_{grastr} \\
&= \lambda_{L1} \mathbb{E}_{x_R \sim p} [\|G_{R \rightarrow M}(x_R) - x_M\|_1] \\
&\quad + \mathbb{E}_{x_R \sim p} [\|\mathcal{G}(G_{R \rightarrow M}(x_R)) - \mathcal{G}(x_M)\|_1] \\
&\quad + \mathbb{E}_{x_R \sim p} [2 - \frac{1}{N-1} \sum_{j=0}^{N-2} \frac{|\sigma_{\mathcal{G}_j(x_M)} \mathcal{G}_j(G_{R \rightarrow M}(x_R))| + C_1}{\sigma_{\mathcal{G}_j(x_M)} \sigma_{\mathcal{G}_j(G_{R \rightarrow M}(x_R))} + C_1} \\
&\quad - \frac{1}{M-1} \sum_{i=0}^{M-2} \frac{|\sigma_{\mathcal{G}_i(x_M)} \mathcal{G}_i(G_{R \rightarrow M}(x_R))| + C_2}{\sigma_{\mathcal{G}_i(x_M)} \sigma_{\mathcal{G}_i(G_{R \rightarrow M}(x_R))} + C_2}]
\end{aligned} \tag{6}$$

where  $\lambda$  is a coefficient for fine tuning;  $\mathcal{L}_{L1}$  is the pixel-wise L1 loss;  $\mathcal{L}_{gral1}$  is the image gradient L1 loss; and  $\mathcal{L}_{grastr}$  is the image gradient structure loss.

### 3.2.2 Adversarial Loss

We employed the adversarial loss [25] in the model to guide the generator to learn high-frequency features, such as style extracted by the discriminator, equation 7, equation 8. In the unsupervised learning process, we only considered the adversarial loss corresponding to the first step generator and ignored the one corresponding to the second step. We have the following:

$$\mathcal{L}_{adv}^{M \rightarrow R} = \mathbb{E}_{x_R \sim p} [\log D_R(x_R)] + \mathbb{E}_{x_M \sim p} [\log(1 - D_R(G_{M \rightarrow R}(x_M)))] \tag{7}$$

$$\mathcal{L}_{adv}^{R \rightarrow M} = \mathbb{E}_{x_M \sim p} [\log D_M(x_M)] + \mathbb{E}_{x_R \sim p} [\log(1 - D_M(G_{R \rightarrow M}(x_R)))] \tag{8}$$

### 3.2.3 Identity Loss

$G_{R \rightarrow M}$  is a mapping from R to M. However, this mapping is a homomorphic mapping because many features only belonging to remote sensing images would be eliminated when a remote sensing image is translated to a map. We hope this mapping can be similar to an isomorphic mapping, whereby the network can output a very similar map when we input a map. Thus, we introduced identity loss derived from identity mapping [40] to improve the structure information mapping of the generator. We have the following:

$$\mathcal{L}_{idt}^{R \rightarrow M} = \mathbb{E}_{x_M \sim p} [\|G_{R \rightarrow M}(x_M) - x_M\|_1] \tag{9}$$

$$\mathcal{L}_{idt}^{M \rightarrow R} = \mathbb{E}_{x_R \sim p} [\|G_{M \rightarrow R}(x_R) - x_R\|_1] \quad (10)$$

### 3.3 Topological Consistency Loss

In contrast to a general image translation task, the map generation task must focus on the topological relationship, which is structural aspect information, of objects on a map. However, the common L1 loss did not consider the topological relationship. We added a topological consistency loss as our optimization objective to optimize the topological relationship of generated maps into the content loss, which consists of the image gradient L1 loss and the image structure loss as follows equation 11:

$$\begin{aligned} \mathcal{L}_{TopoCons}^{R \rightarrow M} &= \mathcal{L}_{gral1} + \mathcal{L}_{grastr} \\ &= \mathbb{E}_{x_R \sim p} [\|\mathcal{G}(G_{R \rightarrow M}(x_R)) - \mathcal{G}(x_M)\|_1] \\ &\quad + \mathbb{E}_{x_R \sim p} \left[ 2 - \frac{1}{N-1} \sum_{j=0}^{N-2} \frac{|\sigma_{\mathcal{G}_j(x_M)} \mathcal{G}_j(G_{R \rightarrow M}(x_R))| + C_1}{\sigma_{\mathcal{G}_j(x_M)} \sigma_{\mathcal{G}_j(G_{R \rightarrow M}(x_R))} + C_1} \right. \\ &\quad \left. - \frac{1}{M-1} \sum_{i=0}^{M-2} \frac{|\sigma_{\mathcal{G}_i(x_M)} \mathcal{G}_i(G_{R \rightarrow M}(x_R))| + C_2}{\sigma_{\mathcal{G}_i(x_M)} \sigma_{\mathcal{G}_i(G_{R \rightarrow M}(x_R))} + C_2} \right] \end{aligned} \quad (11)$$

where  $\mathcal{L}_{gral1}$  is the image gradient L1 loss, and  $\mathcal{L}_{grastr}$  is the image gradient structure loss. Specifically, in our model, the topological consistency loss only works in the generation from a remote sensing image to an online map, which includes the direct translation from a real remote sensing image to an online map at the supervised stage and the translation from a generated remote sensing image to an online map at the unsupervised stage.

#### 3.3.1 Image Gradient L1 Loss

For a map, objects consist of points, lines, curves, and areas rounded by the features and the topological relationship of objects can be presented by the topological relationship of pixels of their outline as well as the edge. The edge curves of objects divide a map tile into different areas for various objects. Thus, we can transform the topological relationship of different objects into the topological relationship of their edge curves.

Hence, we extract the edge curves of a map. The gradient is often used to extract the edge of an image in image processing [41]. Figure 2 shows the generated 3D image of a Google map tile, where the x and y-axis are the length and width of the image, respectively, and the z-axis is the luminance of every pixel. An object with the same color is an isohypsic surface, and its edge consists of points, of which the gradient value is large. Thus, we extract the gradient image of a map as its edge feature. For a  $256 \times 256$  image, we set the pixel value at the point  $(i, j)$  as  $f(i, j)$ . Then the row gradient of

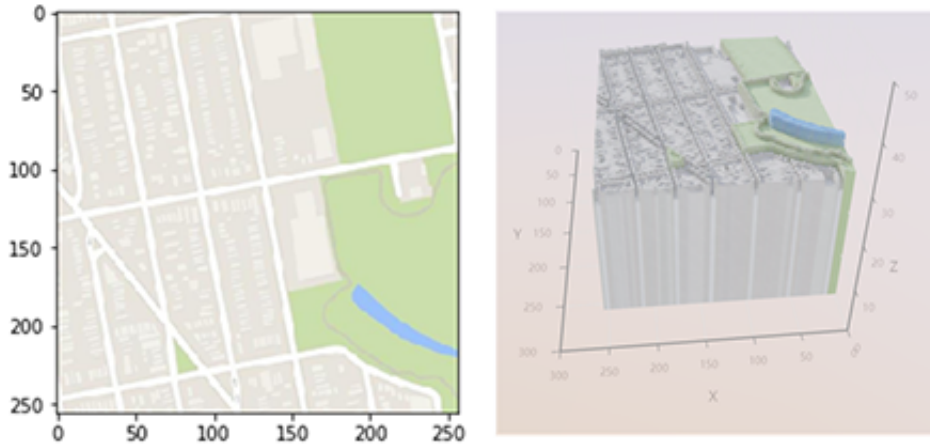


Figure 2: A  $256 \times 256$  google map tile and its 3d map of which the z-axis is luminance.

this point is:

$$g_x(i, j) = f(i, j + 1) - f(i, j) \quad (12)$$

and the column gradient is:

$$g_y(i, j) = f(i + 1, j) - f(i, j) \quad (13)$$

Hence the gradient of this point is:

$$g(i, j) = \sqrt{g_x(i, j)^2 + g_y(i, j)^2} \quad (14)$$

We can then obtain a  $255 \times 255$  matrix  $\mathcal{G}$  consisting of  $g(i, j)$  as the gradient map of the image. Figure 3 presents a Google map tile and its gradient image. The gradient image shows a basic outline of all objects and the outlines divide the gradient image into different areas. Each area is mapped to an object on the map. Each color lump of an object on the map is colored differently, whereas inside its corresponding area on the gradient image is black (all pixel values are 0). Hence, color does not change inside an area but changes only along the edge. Thus, a gradient map can preserve the topological relationships of objects and differences among adjoining objects.

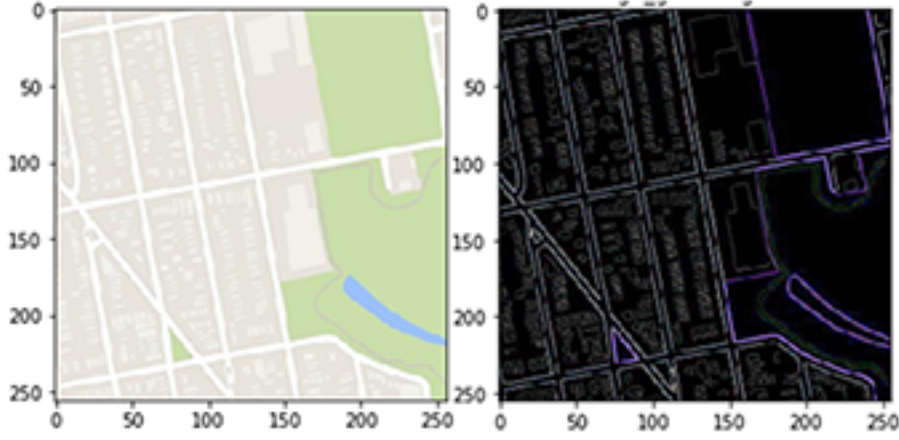


Figure 3: A  $256 \times 256$  google map tile and its  $255 \times 255$  gradient map.

According to the gradient image, we proposed image gradient L1 loss as follows:

$$\mathcal{L}_{grad1} = \mathbb{E}_{x_R \sim p} [\|\mathcal{G}(G_{R \rightarrow M}(x_R)) - \mathcal{G}(x_M)\|_1] \quad (15)$$

where  $\mathcal{G}(x_M)$  is the gradient image of the real map  $x_M$  and  $\mathcal{G}(G_{R \rightarrow M}(x_R))$  is the gradient image of the generated map  $G_{R \rightarrow M}(x_R)$ . By this loss, we hope the generator decreases the L1 distance between image gradient maps of generated maps and their corresponding ground truths. By decreasing this distance, the global gradient as well as the pixel increment among different objects of generated maps can draw near to the ground truths.

### 3.3.2 Image Gradient Structure Loss

However, we have not tackled the topological relationship consistency between generated and real maps. As mentioned before, the topological relationship of objects can be transformed into the topological relationship of edge curves of objects. Furthermore, the topological relationship of edge curves can be transformed into the topological relationship among each point on edge curves of objects, as well as the topological relationship among each point on the gradient image.

For  $255 \times 255$  gradient images of real and generated maps, their pixel matrix  $\mathcal{G}(x_M)$  and  $\mathcal{G}(G_{R \rightarrow M}(x_R))$  have 255 rows and 255 columns. For  $j$ th column ( $i$ th row), pixel values of points on this column (row) comprise an  $i$ -dimension ( $j$ -dimension) random variable  $\mathcal{G}_j(\mathcal{G}_i)$ . For the same column (row) of the generated image and the real map, we hope they are correlative. Due to that possibility, the random variable  $\mathcal{G}_j(\mathcal{G}_i)$  preserves the topological relationship of points in  $\mathcal{G}_j(\mathcal{G}_i)$  by dimensions, and  $\mathcal{G}_j(x_M)$  and  $\mathcal{G}_j(G_{R \rightarrow M}(x_R))$  are highly topological consistent when they are



highly correlative.

We employ the Pearson correlation coefficient to measure the correlation between  $\mathcal{G}_j(x_M)$  and  $\mathcal{G}_j(G_{R \rightarrow M}(x_R))$ , which is as follows:

$$\rho(\mathcal{G}_j(x_M), \mathcal{G}_j(G_{R \rightarrow M}(x_R))) = \frac{\sigma_{\mathcal{G}_j(x_M)\mathcal{G}_j(G_{R \rightarrow M}(x_R))}}{\sigma_{\mathcal{G}_j(x_M)}\sigma_{\mathcal{G}_j(G_{R \rightarrow M}(x_R))}} \quad (16)$$

where  $\sigma_{\mathcal{G}_j(x_M)\mathcal{G}_j(G_{R \rightarrow M}(x_R))}$  is the covariance of  $\mathcal{G}_j(x_M)$  and  $\mathcal{G}_j(G_{R \rightarrow M}(x_R))$ ;  $\sigma_{\mathcal{G}_j(x_M)}$  is the standard deviation of  $\mathcal{G}_j(x_M)$ ; and  $\sigma_{\mathcal{G}_j(G_{R \rightarrow M}(x_R))}$  is the standard deviation of  $\mathcal{G}_j(G_{R \rightarrow M}(x_R))$ .  $\rho(\mathcal{G}_j(x_M), \mathcal{G}_j(G_{R \rightarrow M}(x_R))) \in [-1, 1]$ . When  $\rho$  is closer to 1,  $\mathcal{G}_j(x_M)$  and  $\mathcal{G}_j(G_{R \rightarrow M}(x_R))$  are more correlative.

Due to that the input image is  $M \times N$  scale with  $N$  columns, we calculate the mean value of all  $\rho(\mathcal{G}_j(x_M), \mathcal{G}_j(G_{R \rightarrow M}(x_R)))$ :

$$\rho(\mathcal{G}_j(x_M), \mathcal{G}_j(G_{R \rightarrow M}(x_R)))_{mean} = \frac{1}{N-1} \sum_{j=0}^{N-2} \frac{\sigma_{\mathcal{G}_j(x_M)\mathcal{G}_j(G_{R \rightarrow M}(x_R))}}{\sigma_{\mathcal{G}_j(x_M)}\sigma_{\mathcal{G}_j(G_{R \rightarrow M}(x_R))}} \quad (17)$$

We have:

$$\rho(\mathcal{G}_i(x_M), \mathcal{G}_i(G_{R \rightarrow M}(x_R)))_{mean} = \frac{1}{M-1} \sum_{i=0}^{M-2} \frac{\sigma_{\mathcal{G}_i(x_M)\mathcal{G}_i(G_{R \rightarrow M}(x_R))}}{\sigma_{\mathcal{G}_i(x_M)}\sigma_{\mathcal{G}_i(G_{R \rightarrow M}(x_R))}} \quad (18)$$

for all rows. Thus, we proposed the image gradient structure loss:

$$\begin{aligned} \mathcal{L}_{grastr} = \mathbb{E}_{x_R \sim p} [ & 2 - \frac{1}{N-1} \sum_{j=0}^{N-2} \frac{|\sigma_{\mathcal{G}_j(x_M)\mathcal{G}_j(G_{R \rightarrow M}(x_R))}| + C_1}{\sigma_{\mathcal{G}_j(x_M)}\sigma_{\mathcal{G}_j(G_{R \rightarrow M}(x_R))} + C_1} \\ & - \frac{1}{M-1} \sum_{i=0}^{M-2} \frac{|\sigma_{\mathcal{G}_i(x_M)\mathcal{G}_i(G_{R \rightarrow M}(x_R))}| + C_2}{\sigma_{\mathcal{G}_i(x_M)}\sigma_{\mathcal{G}_i(G_{R \rightarrow M}(x_R))} + C_2} ] \end{aligned} \quad (19)$$

where  $C_1$  and  $C_2$  are constant to keep loss stable when  $|\sigma_{\mathcal{G}_j(x_M)\mathcal{G}_j(G_{R \rightarrow M}(x_R))}|$  or  $|\sigma_{\mathcal{G}_i(x_M)\mathcal{G}_i(G_{R \rightarrow M}(x_R))}|$  is very close to 0. When this loss is decreasing, the correlation of each column and each row of the gradient images of the generated map and the real map is increasing. Consequently, the generator can improve topological consistency between the generated and the real maps.

### 3.4 Model Implements

#### 3.4.1 Network Architecture

Inspired by the design in [17], S<sup>2</sup>OMGAN builds its generators with the 9-ResNet-Blocks architecture and PatchGANs [17, 21] discriminators with a size of 70, which show impressive performance for the img2img translation. Specifically, the generator network consists of two downsampling convolutional layers with 2-stride, nine residual blocks [42] and the following two transposed convolutional layers of similar stride for upsampling. Instance normalization [40] is leveraged in the generator but not in the discriminator.

#### 3.4.2 Avoid Steganography During Unsupervised Stage

[43] revealed that the CycleGAN model tends to add high-frequency noise to hide information in intermediate results to achieve improved reconstruction. To avoid unnecessary noise, we set up a trick during our training. Specifically, we apply cycle-consistency to extend the availability of unpaired training, which causes models to learn steganography. Although this feature helps the generator recover the original image in the work based on cycle-consistency, steganography brings noise that interrupts the correct structure feature of the maps in our map-generated task. To avoid this issue, we freeze the weight of the first step generator in the two-step cycle reconstruction, which tends to learn steganography, when training in the unsupervised stage. This rule will be activated after several epochs (we denote the threshold as  $t_s$ ), which allows cycle-consistency to help accelerate model convergence early on.

### 3.5 Topological Consistency Measurement: ESSI

Traditional image quality assessment, including MSE and SSIM, can be introduced to assess the quality of generated maps. MSE can measure the global pixel-wise similarity between generated maps and their corresponding ground truth, whereas SSIM can measure the similarity of luminance, contrast, and structure between generated maps and their ground truth. However, besides MSE and SSIM, we hope to employ a suitable metric to measure the topological consistency between a generated and a real map. In Section 3.3, we discussed that the topological relationship of objects on maps can be preserved by edge curves of objects. Based on this situation, we proposed edge structural similarity index (ESSI):

$$ESSI(G(x_R), x_M) = \frac{(|\sigma_{\mathcal{E}(G(x_R))\mathcal{E}(x_M)}| + C_1)(2\mu_{\mathcal{E}(G(x_R))}\mu_{\mathcal{E}(x_M)} + C_2)}{(\sigma_{\mathcal{E}(G(x_R))}\sigma_{\mathcal{E}(x_M)} + C_1)(\mu_{\mathcal{E}(G(x_R))}^2 + \mu_{\mathcal{E}(x_M)}^2 + C_2)} \quad (20)$$

#### 3.5.1 Topological Consistency Measurement Through the Correlation Coefficient

We apply the Canny edge detector [41] to extract edge images of the generated map and its ground truth, and dimensionality reduce their  $M \times N$  pixel value matrix into  $M \times N$ -dimension vectors by progressive scanning method. Each point in the pixel value matrix has its coordinate of row and column numbers, which preserves its topological relationship with other points. After reduction, the reduced vector keeps topological relationship among points because each coordinate of points would only be mapped to only one dimension of the vector, and each dimension of the vector is mapped to only one coordinate. This vector can be seen as a  $M \times N$ -dimension random variable. The topological relationship of objects is then transformed to the order of the random variable, and the topological consistency between the generated map and the ground truth is transformed to the correlation between the random variables  $\mathcal{E}(G(x_R))$  and  $\mathcal{E}(x_M)$  of their edge images.

The absolute value of Pearson correlation coefficient between these two edge images is employed to measure the correlation:

$$\rho(G(x_R), x_M) = \frac{|\sigma_{\mathcal{E}(G(x_R))\mathcal{E}(x_M)}| + C_1}{\sigma_{\mathcal{E}(G(x_R))}\sigma_{\mathcal{E}(x_M)} + C_1} \quad (21)$$

where  $\sigma_{\mathcal{E}(G(x_R))}$  and  $\sigma_{\mathcal{E}(x_M)}$  are the standard deviation of  $\mathcal{E}(G(x_R))$  and  $\mathcal{E}(x_M)$ , respectively;  $\sigma_{\mathcal{E}(G(x_R))\mathcal{E}(x_M)}$  is the covariance between  $\mathcal{E}(G(x_R))$  and  $\mathcal{E}(x_M)$ ; and  $C_1$  is a constant to keep  $\rho(G(x_R), x_m)$  stable when  $\sigma_{\mathcal{E}(G(x_R))}\sigma_{\mathcal{E}(x_M)}$  is close to 0.

#### 3.5.2 Avoid Wrong Evaluation by Adding GMS

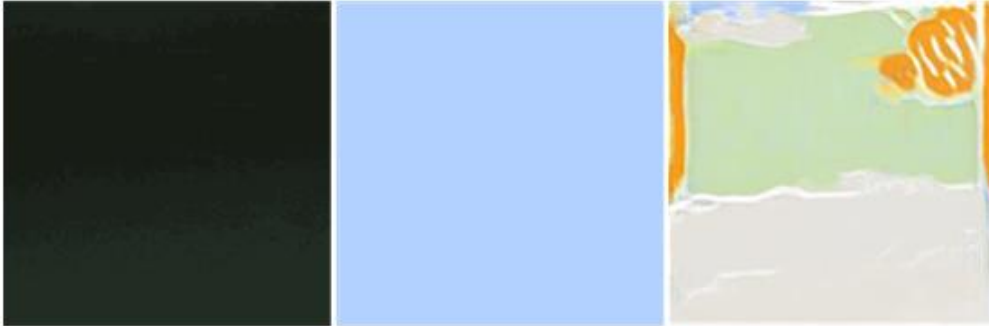


Figure 4: From left to right are the remote sensing image of the sea, its corresponding google map tile, and the wrongly generated map. Obviously, the generated map is poor but  $\rho(G(x_R), x_m)$  is very high because the edge matrix of the map tile is 0 matrix.

However, in our experiment, an overestimation would happen if only we use  $\rho(G(x_R), x_m)$  to evaluate the generated maps. As Figure 4 shows, if  $G(x_R)$  is wrongly generated such that  $\mathcal{E}(G(x_R)) \neq 0$  while  $\mathcal{E}(x_M) = 0$ , then  $\sigma_{\mathcal{E}(G(x_R))\mathcal{E}(x_M)}$  and  $\sigma_{\mathcal{E}(G(x_R))}\sigma_{\mathcal{E}(x_M)}$  equal to 0, but  $\rho(G(x_R), x_m)$  equals to 1. Thus  $G(x_R)$  would be wrongly evaluated to be very good. To avoid this case, we constructed a

coefficient that is inspired by the gradient magnitude similarity (GMS) proposed in [38]:

$$\theta(G(x_R), x_M) = \frac{2\mu_{\mathcal{E}(G(x_R))}\mu_{\mathcal{E}(x_M)} + C_2}{\mu_{\mathcal{E}(G(x_R))}^2 + \mu_{\mathcal{E}(x_M)}^2 + C_2} \quad (22)$$

where  $\mu_{\mathcal{E}(G(x_R))}$  and  $\mu_{\mathcal{E}(x_M)}$  are the mean values of  $\mathcal{E}(G(x_R))$  and  $\mathcal{E}(x_M)$ , respectively. Thus, when  $\mathcal{E}(x_M)$  is 0 matrix and  $\mathcal{E}(G(x_R))$  is not, we have the following:

$$\begin{aligned} \sigma_{\mathcal{E}(G(x_R))\mathcal{E}(x_M)} &= \sigma_{\mathcal{E}(G(x_R))}\sigma_{\mathcal{E}(x_M)} = 0 \\ \rho(G(x_R), x_M) &= 1 \\ 2\mu_{\mathcal{E}(G(x_R))}\mu_{\mathcal{E}(x_M)} &= 0 \\ \mu_{\mathcal{E}(G(x_R))}^2 + \mu_{\mathcal{E}(x_M)}^2 &= \mu_{\mathcal{E}(G(x_R))}^2 \\ \theta(G(x_R), x_M) &= \frac{2\mu_{\mathcal{E}(G(x_R))}\mu_{\mathcal{E}(x_M)} + C_2}{\mu_{\mathcal{E}(G(x_R))}^2 + \mu_{\mathcal{E}(x_M)}^2 + C_2} = \frac{C_2}{\mu_{\mathcal{E}(G(x_R))}^2 + C_2} \end{aligned} \quad (23)$$

By setting  $C_2$  appropriately, we can make  $\theta$  very close to 0. When  $\mathcal{E}(x_M) = 0$ , and  $G(x_R)$  is well generated, then  $\mathcal{E}(G(x_R)) = 0$ ,  $\theta = 1$ . Then, we can obtain ESSi:

$$\begin{aligned} ESSi(G(x_R), x_M) &= \theta(G(x_R), x_M)\rho(G(x_R), x_M) \\ &= \frac{(|\sigma_{\mathcal{E}(G(x_R))\mathcal{E}(x_M)}| + C_1)(2\mu_{\mathcal{E}(G(x_R))}\mu_{\mathcal{E}(x_M)} + C_2)}{(\sigma_{\mathcal{E}(G(x_R))}\sigma_{\mathcal{E}(x_M)} + C_1)(\mu_{\mathcal{E}(G(x_R))}^2 + \mu_{\mathcal{E}(x_M)}^2 + C_2)} \end{aligned} \quad (24)$$

This metric is symmetric, such that  $ESSi(G(x_R), x_M) = ESSi(x_M, G(x_R))$ , bounded that  $ESSi \in [0, 1]$ , and  $ESSi = 1$  if and only if when  $M \times N$  dimension vector  $\mathcal{E}(G(x_R)) = \mathcal{E}(x_M)$ ,  $C \neq 0$ .



Figure 5: Input remote sensing image, two generated maps by different model and their corresponding Google tilemap (ground truth). The output of  $S^2OMGAN$  (Paired only) has MSE of 148.50, SSIM of 0.9531 and ESSi of 0.3036. By contrast, the generated map of  $S^2OMGAN$  has MSE of 169.41, SSIM of 0.9482 and ESSi of 0.4299. Although the second map outperformed the third for MSE and SSIM, the third generates a map with higher ESSi and better topological relationships from a human visual perspective.

### 3.5.3 Advantage of ESSi Compared to MSE and SSIM

ESSi outperforms MSE and SSIM in measuring topological consistency. Figure 5 presents two generated maps of the same raw image by different models. The generated map generated by  $S^2OMGAN$  (paired only, which means only trained on paired training samples) obtains MSE score of 148.50 and SSIM score of 0.9531, which are better than the output of  $S^2OMGAN$  (trained on all training samples) with MSE score of 169.41 and SSIM score of 0.9482. From the MSE and SSIM scores, the second image has better quality than the third. However, from the human visual perspective, the third image has good topological relationship of objects. The third image presented a clear road on the top right corner and no blur on the grass. ESSi fits the human visual perspective more than MSE and SSIM when evaluating the topological relationship of the two images (ESSi of the second image is 0.3036 while the third is 0.4299).

The calculation method of MSE and SSIM results in this phenomenon. The blurred part of the second

map has high approximate pixel value with the corresponding Google map tile, which increases MSE and SSIM. However, these blurred parts only decreased ESSI due to a fault of the topological relationship, which resulted in blur.

Figure 6 shows the edge images of the output of  $S^2$ OMGAN (paired only) and  $S^2$ OMGAN, and their

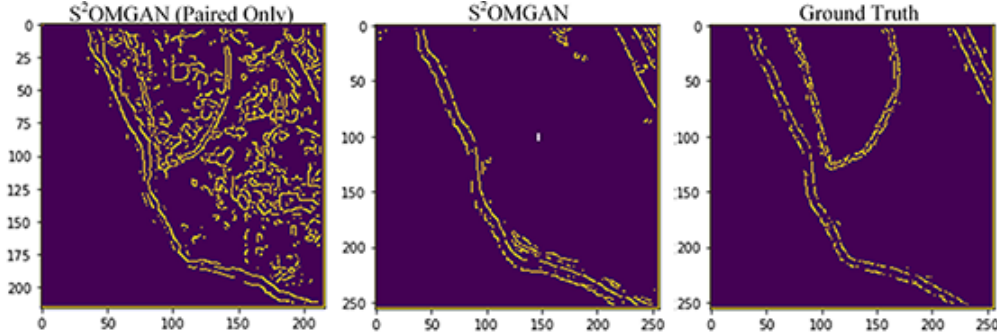


Figure 6: Edge images of generated maps of different models and the ground truth. Edge images extract topological relationships more precisely with low influence of blur.

corresponding ground truths. The blurred parts of the generated map of  $S^2$ OMGAN (paired only) led to much more edge curves than the ground truth, which resulted in wrong topological consistency. Calculation of ESSI is based on the edge image, which seizes the topological relationship of objects more accurately with lower influence of blur. Thus, the topological consistency of generated maps can be evaluated precisely by ESSI.

## 4 Experiments and Results

### 4.1 Datasets and Baseline

#### 4.1.1 Datasets

We conducted our experiments on two datasets related to online map generating:

**Aerial photograph**  $\leftrightarrow$  **Maps** [19]: This dataset consists of 2194 aerial images and their corresponding online maps scraped from Google maps. All samples are about the places in and around New York City.

**Simple styled maps**  $\leftrightarrow$  **Target styled maps** [5]: This dataset consist of around 1,088 simple styled maps tiles at zoom 15 generated from OSM vector data and 1,088 target styled maps matching the simple styled ones. In this dataset, simple styled maps are used as input. Differing from rendering from vector data, the inputs are also images. We utilized this dataset to conduct experiment to check the applicability of the model among all online maps generating tasks.

All these datasets were shuffled and randomly separated into paired and the unpaired parts by different paired-ratio, and then were divided into training sets and testing sets. Specifically, we set the paired-ratio as 10% and 50% to check how our model performed at different semi-supervised levels. Final datasets with different paired-ratio but same source dataset shared the same testing set. In our training set, each remote sensing image in the paired part has a corresponding maps. Neither any remote sensing image nor any map has its corresponding image from the opposed domain in the unpaired part.

#### 4.1.2 Baseline

We compared  $S^2$ OMGAN with five SOTA methods we mentioned in Section 2, namely, Pix2Pix [16], CycleGAN [17], UNIT [18], AttentionCycleGAN [19] and GeoGAN [20]. Due to the limitation that Pix2Pix and GeoGAN could only be trained in a supervised manner, we run them on the paired part of our dataset to see their performance. To perform a comparison, we trained  $S^2$ OMGAN only on the same paired part. For other models, we fed all samples to them in their acceptable methods.

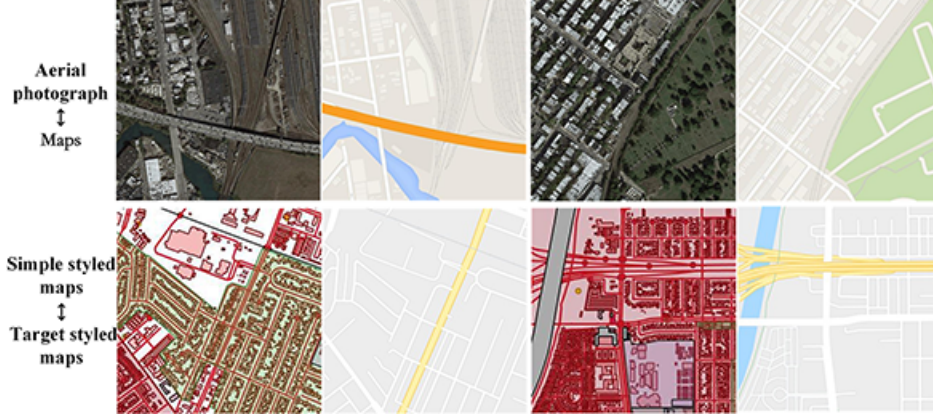


Figure 7: Samples of two types of dataset.

## 4.2 Metrics

We employed objective and subjective metrics to measure the quality of generated maps. As each generated map has a corresponding ground truth, we applied traditional full-reference image quality assessment, including MSE and SSIM. Also the new full-reference image quality assessment ESSI proposed by us was employed to measure topological consistency between the output map and its ground truth.

### 4.2.1 Objective Metrics

**MSE:** We used MSE as the first metric to measure the output images because it is commonly used in the image processing task. MSE is as follows:

$$MSE(G(x_R), x_M) = \frac{1}{M \times N} \sum_{i=0}^{M-1} \sum_{j=0}^{N-1} (p_{G(x_R)}(i, j) - p_{x_M}(i, j))^2 \quad (25)$$

where  $M$  and  $N$  is the length and width of the image, respectively; and  $p_{G(x_R)}(i, j)$  and  $p_{x_M}(i, j)$  are the pixel values at the pixel  $(i, j)$  of the generated map  $G(x_R)$  and the real map  $x_M$ , respectively.

**SSIM:** We used SSIM to measure the structural similarity between the generated map and its ground truth. SSIM is as follows:

$$SSIM(G(x_R), x_M) = \frac{(2\mu_{G(x_R)}\mu_{x_M} + C_1)(2\sigma_{G(x_R)x_M} + C_2)}{(\mu_{G(x_R)}^2 + \mu_{x_M}^2 + C_1)(\sigma_{G(x_R)}^2 + \sigma_{x_M}^2 + c_2)} \quad (26)$$

where  $\mu_{G(x_R)}$  and  $\mu_{x_M}$  are the means of  $G(x_R)$  and  $x_M$ , respectively;  $\sigma_{G(x_R)}^2$  and  $\sigma_{x_M}^2$  are the variances of  $G(x_R)$  and  $x_M$ , respectively;  $\sigma_{G(x_R)x_M}$  is the covariance between  $G(x_R)$  and  $x_M$ ; and  $C_1$  and  $C_2$  are the constants to keep the metric stable when  $\mu_{G(x_R)}^2 + \mu_{x_M}^2$  and  $\sigma_{G(x_R)}^2 + \sigma_{x_M}^2$  is close to 0.

**ESSI:** We used the ESSI proposed in Section 3.5 as our metric as well. ESSI is as follows:

$$ESSI(G(x_R), x_M) = \frac{(|\sigma_{\mathcal{E}(G(x_R))\mathcal{E}(x_M)}| + C_1)(2\mu_{\mathcal{E}(G(x_R))}\mu_{\mathcal{E}(x_M)} + C_2)}{(\sigma_{\mathcal{E}(G(x_R))}\sigma_{\mathcal{E}(x_M)} + C_1)(\mu_{\mathcal{E}(G(x_R))}^2 + \mu_{\mathcal{E}(x_M)}^2 + C_2)} \quad (27)$$

where  $\sigma_{\mathcal{E}(G(x_R))}$  and  $\sigma_{\mathcal{E}(x_M)}$  are the standard deviation of  $\mathcal{E}(G(x_R))$  and  $\mathcal{E}(x_M)$ , respectively;  $\sigma_{\mathcal{E}(G(x_R))\mathcal{E}(x_M)}$  is the covariance between  $\mathcal{E}(G(x_R))$  and  $\mathcal{E}(x_M)$ ;  $C_1$  is a constant to keep ESSI stable when  $\sigma_{\mathcal{E}(G(x_R))}\sigma_{\mathcal{E}(x_M)}$  is close to 0;  $\mu_{\mathcal{E}(G(x_R))}$  and  $\mu_{\mathcal{E}(x_M)}$  are the mean values of  $\mathcal{E}(G(x_R))$  and  $\mathcal{E}(x_M)$ , respectively;  $C_2$  is a constant to keep metric stable when  $\mu_{\mathcal{E}(G(x_R))}^2 + \mu_{\mathcal{E}(x_M)}^2$  is close to 0.

### 4.2.2 Subjective Metric

As the result of objective metrics could not fit human visual system completely, we designed a human perceptual test to check if our model generates more valid online maps than baselines. We randomly



picked participants from graduates majoring in GIS and built up a web application as a platform to conduct the quality assessment for all models on the four datasets, which contained 290, 290, 515, and 515 samples. The platform offered the participants a website that presents a multiple-choice question containing eight pictures randomly picked from one of the four datasets for each time, namely, input image, ground truth online map corresponding to the input, and online maps generated from input by six models. These six models included five baselines and our S<sup>2</sup>OMGAN trained with semi-supervised setup on full data. The participants should select relatively the best results and the ones that could best describe the input and is most similar to the ground truth among the six models. Meanwhile, the system would count the frequency that every model is selected. Finally, the statistics reveals the performance of every model.

### 4.3 Experiment Setup

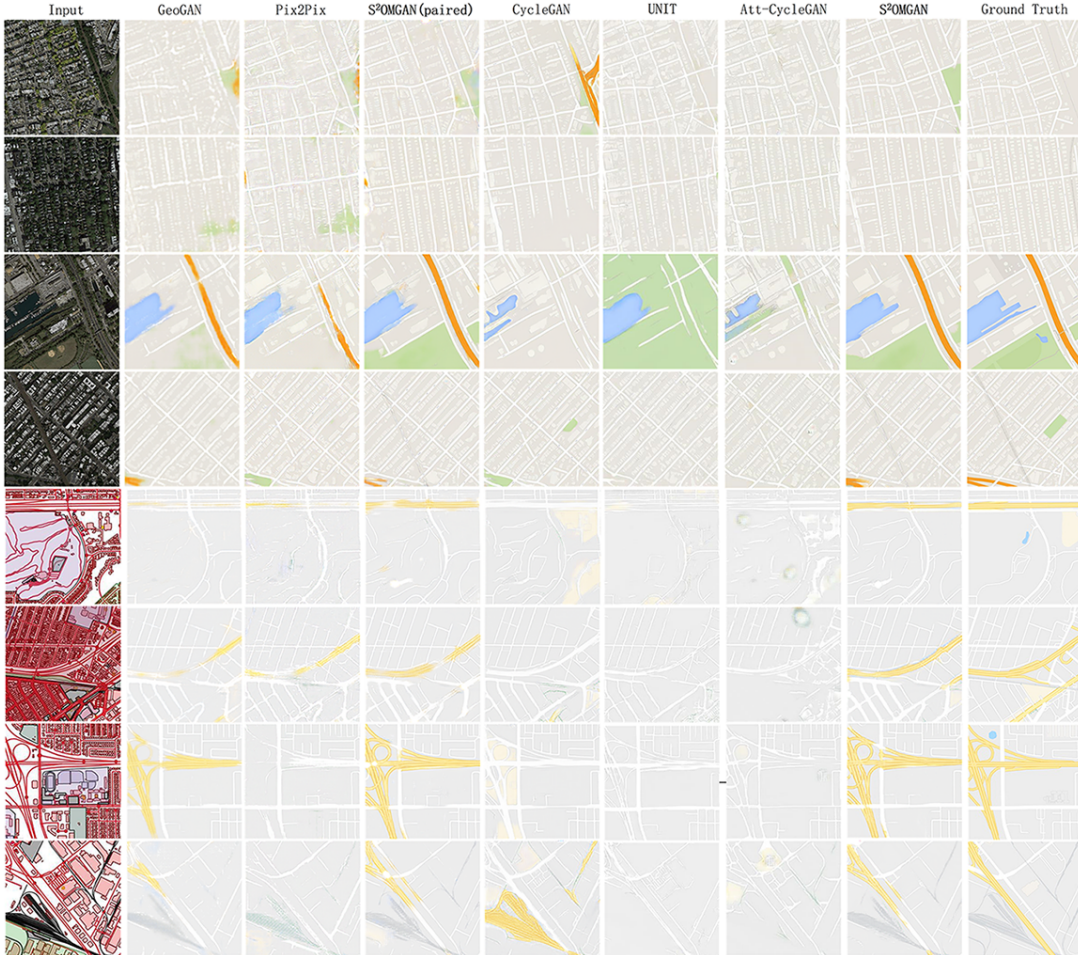


Figure 8: Some selected samples of each dataset in comparison experiment. Every two rows correspond with one of four datasets listed in 4.1. Each row includes the input image, maps generated by five baselines and S<sup>2</sup>OMGAN, and the ground truth. Specifically, the maps generated by S<sup>2</sup>OMGAN trained on only paired data and all data are presented respectively in each row.

For all the experiments, we set  $\lambda_{ctn} = 10$ ,  $\lambda_{adv} = 1$ ,  $\lambda_{idt} = 0.1$  in Formulation equation 1,  $\lambda_{L1u} = 1$  in Formulation equation 3 and equation 4, and  $\lambda_{L1} = 10$  in Formulation equation 5 and equation 6. We adopted a 1 batch size Adam optimizer [44] with  $\beta_1 = 0.5$ ,  $\beta_2 = 0.999$  and a two-stage learning rate strategy used in [17]. We trained the model for 200 epochs on each dataset and  $t_s$  was set to 150. For metrics, in SSIM (Formulation equation 26) we set  $C_1 = C_2 = 1e^{-12}$ . By contrast, in ESSI (Formulation equation 27) we set  $C_1 = C_2 = 1e^{-12}$ . We both calculated objective metrics by the

luminance of the output and the mean value of that by three channels (R, G, B) to present results globally.

## 4.4 Results

### 4.4.1 Qualitative Result

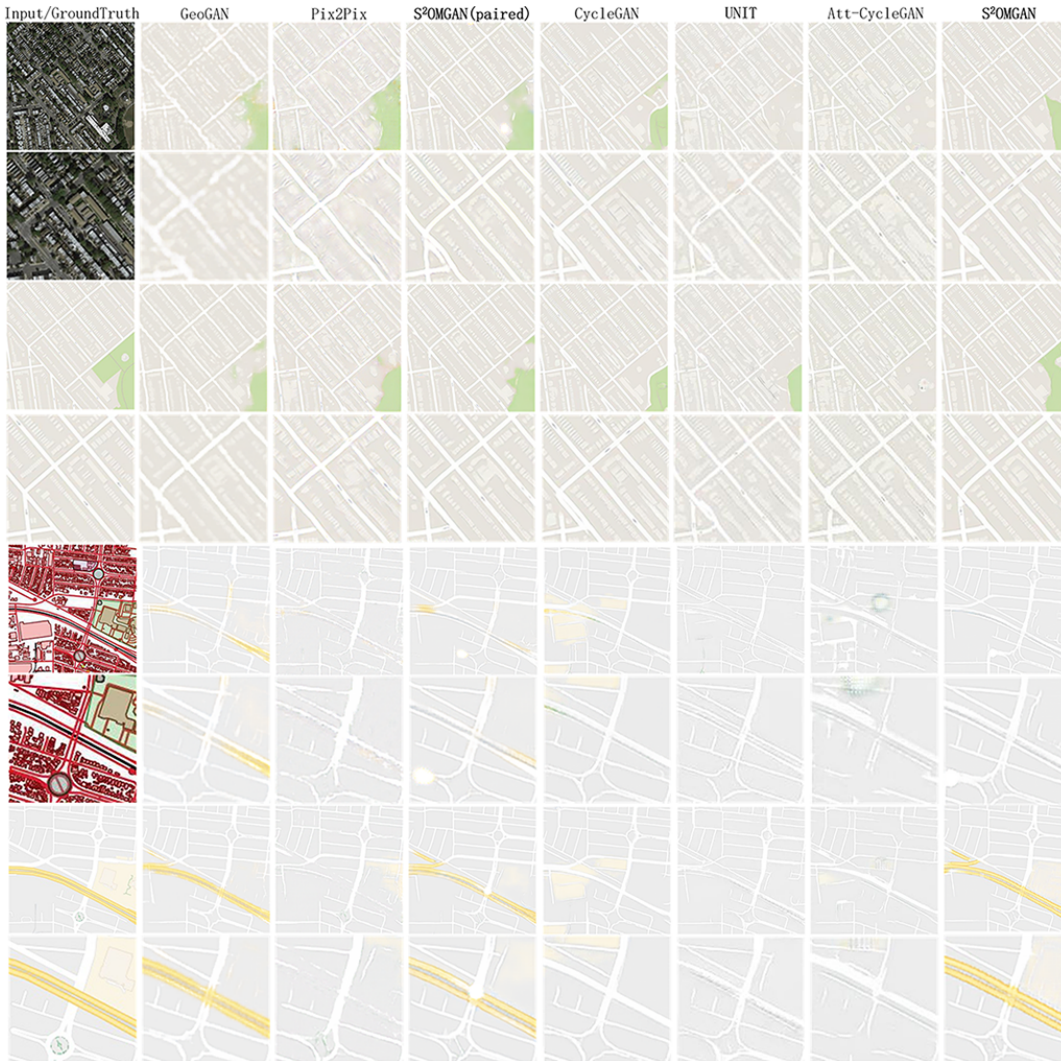


Figure 9: Selected samples of each source datasets in comparison experiment. Every four rows correspond with one of two source datasets. The first column of each four rows consists of the full-size input image, magnified area (show structure feature) of the input image, full-size ground truth and magnified area of ground truth. The first two rows of other columns list the maps and their magnified area generated by each model trained on a 10% paired-ratio training set and the two rows below list the maps and their magnified area generated by each model trained on 50% paired-ratio training set.

Figure 8 and Figure 9 show the qualitative comparison among five baselines and our S<sup>2</sup>OMGAN model. In comparison to GeoGAN and Pix2Pix, our model trained by only paired data performed better on generating structure features such as continuous color blocks and regular border shape. In comparison to the other four unsupervised models, besides obtaining better structure similarity, our S<sup>2</sup>OMGAN trained with all data did a better job of distinguishing different features and filling in corresponding colors. Furthermore, the model trained on all data beat the one trained by only paired data and reached the best performance thanks to the semi-supervised learning strategy carried on

paired and unpaired data. In addition, using more paired data in the training period contributed to better results as we expected.

#### 4.4.2 Quantitative Result

Table 1: MSE (smaller the better)

Model\Dataset	A-10%		A-50%		B-10%		B-50%	
	RGBmean	Luminance	RGBmean	Luminance	RGBmean	Luminance	RGBmean	Luminance
GeoGAN	0.7363	0.7534	0.7889	0.8008	0.8408	0.8483	0.8606	0.8667
Pix2Pix	0.6657	0.6862	0.6998	0.7243	0.8029	0.8108	0.8249	0.8318
$S^2OMGAN$ (paired)	0.7419	0.7572	0.7915	0.8029	0.8432	0.8506	0.8644	0.8698
CycleGAN	0.714	0.7273	0.7166	0.7287	0.6802	0.688	0.6893	0.6968
UNIT	0.639	0.6534	0.7003	0.7155	0.716	0.7217	0.8039	0.8105
Att-CycleGAN	0.6568	0.6709	0.6708	0.6836	0.627	0.6318	0.671	0.676
$S^2OMGAN$	<b>0.7515</b>	<b>0.7651</b>	<b>0.7993</b>	<b>0.8105</b>	<b>0.8443</b>	<b>0.8511</b>	<b>0.8665</b>	<b>0.872</b>

Table 2: SSIM (as close to 1 as better)

Model\Dataset	A-10%		A-50%		B-10%		B-50%	
	RGBmean	Luminance	RGBmean	Luminance	RGBmean	Luminance	RGBmean	Luminance
GeoGAN	0.7363	0.7534	0.7889	0.8008	0.8408	0.8483	0.8606	0.8667
Pix2Pix	0.6657	0.6862	0.6998	0.7243	0.8029	0.8108	0.8249	0.8318
$S^2OMGAN$ (paired)	0.7419	0.7572	0.7915	0.8029	0.8432	0.8506	0.8644	0.8698
CycleGAN	0.714	0.7273	0.7166	0.7287	0.6802	0.688	0.6893	0.6968
UNIT	0.639	0.6534	0.7003	0.7155	0.716	0.7217	0.8039	0.8105
Att-CycleGAN	0.6568	0.6709	0.6708	0.6836	0.627	0.6318	0.671	0.676
$S^2OMGAN$	<b>0.7515</b>	<b>0.7651</b>	<b>0.7993</b>	<b>0.8105</b>	<b>0.8443</b>	<b>0.8511</b>	<b>0.8665</b>	<b>0.872</b>

Table 3: ESSI (as close to 1 as better)

Model\Dataset	A-10%		A-50%		B-10%		B-50%	
	RGBmean	Luminance	RGBmean	Luminance	RGBmean	Luminance	RGBmean	Luminance
GeoGAN	0.1758	0.186	0.2541	0.2661	0.3961	0.3995	0.4464	0.4502
Pix2Pix	0.137	0.1475	0.1879	0.2047	0.3229	0.3277	0.3617	0.3673
$S^2OMGAN$ (paired)	0.2162	0.2278	0.2916	0.3071	0.4076	0.4124	0.4557	0.4605
CycleGAN	0.2025	0.2179	0.2084	0.2215	0.015	0.0185	0.0253	0.0294
UNIT	0.0881	0.0939	0.1703	0.1787	0.1572	0.1594	0.3196	0.3199
Att-CycleGAN	0.1418	0.1509	0.0881	0.166	0.073	0.0725	0.0309	0.0328
$S^2OMGAN$	<b>0.239</b>	<b>0.2553</b>	<b>0.3043</b>	<b>0.3234</b>	<b>0.427</b>	<b>0.4289</b>	<b>0.46</b>	<b>0.4652</b>

Similar to qualitative results, objective and subjective metrics results show that our  $S^2OMGAN$  outperforms other baseline models. Table 1, 2, and 3 show objective metrics comparison among all the models while Table 4 shows the result of the subjective metric.

First, we discuss the results of objective metrics. For MSE,  $S^2OMGAN$  perform a little worse than GeGAN. However, as discussed in 3.5, MSE can only measure the global mean distance of pixel values between a generated map and its ground truth, which has a great flaw in this task.

Besides, we could see that  $S^2OMGAN$  outperforms SOTA baselines in SSIM and ESSI assessment. Especially, significant improvement is presented at ESSI, which indicates the improvement of quality of topological relationship among objects on generated maps by considering the topological consistency in our method.

Meanwhile, the model trained with a semi-supervised strategy obtained better result than one trained with only paired data and other unsupervised baselines, which proves the effectiveness of our semi-supervised strategy. In other words, the semi-supervised strategy takes the advantage of unpaired data to provide more valid information to learn, and takes the advantage of paired data to offer accurate target for training.



Table 4: Result of subjective metric (%)

Dataset/Model	GeoGAN	Pix2Pix	CycleGAN	UNIT	Att-CycleGAN	$S^2OMGAN$
A-10%	1.03	1.86	30.57	3.73	9.57	<b>53.24</b>
A-50%	5.52	7.81	18.77	2.68	4.73	<b>60.49</b>
B-10%	10.62	6.74	19.66	13.34	1.58	<b>48.06</b>
B-50%	12.55	10.88	10.77	8.58	3.03	<b>54.18</b>

Then, we analyze the result of the subjective metric. In the human perceptual test, every sample was assessed over 3 times on average and the the number of participant is 145 person-time. With 10% and 50% paired data on dataset A, our model gained 53.24% and 60.49% support respectively. And with 10% and 50% paired data on dataset B, our model gained 48.06% and 54.18% support respectively. Obviously, our model dominates the human perceptual test. This result reports that our  $S^2OMGAN$  outperforms the SOTA baselines during human perceptual judgement.

#### 4.5 Ablation Study

Content loss consists of three parts: L1 loss, image gradient L1 loss and image gradient structure loss. The experimental result shows that our model with content loss including L1 loss, image gradient L1 loss and image gradient structure loss performed better than models using content loss with only L1 loss (CycleGAN and Pix2pix). In order to test these losses in the same model to discuss the impact of different losses on generated maps, we conducted an ablation study. We compared against ablations of



Figure 10: Selected three samples from the results of the ablation study conducted on dataset A-50%. Each sample included the ground truth and the maps generated by models trained with full loss function, L1 loss alone, proposed structure constrain alone, L1 loss and Gradient structure loss, and L1 loss and Gradient L1 loss.

the content loss on dataset A-50%. Figure 10 shows the qualitative effect of the three components of content loss. We could see that structure quality, such as color-continuity, is not good when L1 Loss is used alone, which is adopted in universal img2img work. We then tried using only GraStr Loss and GraL1 Loss proposed in this work when training our model. In this case, the model only focuses to generate maps that have similar objects outline as the ground truths, but not penalizes the mismatch on feature colors between them, which is the symbol of types of object features. Therefore, erroneous objects classifying happens, although topological relationships of objects on generated maps are more similar to the real scenario. To further find how the two specific types of topological consistency loss work, we conducted a test with each of the two losses removed. We find that removing GraL1 Loss results in bad color continuity and blurring outline, whereas disabling GraStr Loss makes the model fail to generate the maps with correct topological relationships of objects. The phenomenon claims that image GraL1 Loss and GraStr Loss guide the model to learn pixel-level continuity and topological consistency, respectively.

We performed a quantitative ablation study for various losses combination. The result is presented in Table 5, 6 and 7, and we only present results of luminance to simplify analysis. Table 5 shows the result of the ablation study of L1 loss, which indicates that GraStr Loss and

Table 5: Comparison of objective metrics of L1 loss’s ablation study.

<b>Component\Metric</b>	<b>MSE</b>	<b>SSIM</b>	<b>ESSI</b>
Full	83.77	0.8105	0.3234
L1	95.8	0.7915	0.2956
L1&GraStr	83.97	0.8105	0.3227
L1&GraL1	90.11	0.7942	0.3034

GraL1 Loss contribute to increasing all objective metrics. Furthermore, GraStr outperforms GraL1 to improve the global quality of generated maps. GraStr improves the SSIM and ESSI scores significantly, which implies that GraStr greatly helps the generator to improve the topological relationship of objects on generated maps. This improvement enhances global pixel-wise consistency, which the drop of MSE score presents. Meanwhile, the slight improvement of all metrics after adding GraL1 shows that GraL1 fine tuned the quality of generated maps.

Table 6 shows the result of the ablation study of image gradient L1 loss. Compared to Table 5, the

Table 6: Comparison of objective metrics of image gradient L1 loss’s ablation study.

<b>Component\Metric</b>	<b>MSE</b>	<b>SSIM</b>	<b>ESSI</b>
Full	83.77	0.8105	0.3234
GraL1	210.39	0.73	0.2379
GraStr& GraL1	193.66	0.7999	0.3229
L1&GraL1	90.11	0.7942	0.3034

single GraL1 loss performs very poorly under all objective metrics. When GraStr was combined with GraL1, SSIM and ESSI increased greatly and MSE increased a little, which proves the contribution of GraStr to improve the topological relationship of objects on generated maps, as what has been discussed for Table 5. L1 loss improves global pixel-wise consistency, which the drop of MSE shows. This improvement contributes to the rise of SSIM and ESSI. Thus, L1 is a vital loss to guide the generator to keep pixel-wise consistency, which is a primary constraint for the map translation task.

Table 7: Comparison of objective metrics of image gradient structure loss’s ablation study.

<b>Component\Metric</b>	<b>MSE</b>	<b>SSIM</b>	<b>ESSI</b>
Full	83.77	0.8105	0.3234
GraStr	162.81	0.7996	0.3222
GraStr&GraL1	193.66	0.7999	0.3229
L1&GraStr	83.97	0.8105	0.3227

Table 7 shows the result of the ablation study of the image gradient structure loss. Single GraStr obtains high SSIM and ESSI, which indicates the importance of GraStr to improve the topological relationship of objects on generated maps. However, a high MSE shows the flaw of GraStr to keep pixel-wise consistency, which can be improved by adding L1 loss. Meanwhile, by adding GraL1, all objective metrics improve slightly, proving its fine tuning function again.

In conclusion, the ablation study shows different effects of L1 loss, GraStr loss, and GraL1 loss. L1 loss and GraStr loss are important for the generator because L1 loss constrains the generator to decrease the global pixel-wise distance between the output and the ground truth while GraStr loss constrains the generator to improve the topological consistency between the output and the ground truth. GraL1 loss can fine tune the quality of generated maps under the constraint of L1 loss and GraStr loss. The quantitative result is consistent with the qualitative result.

## 4.6 Discussion

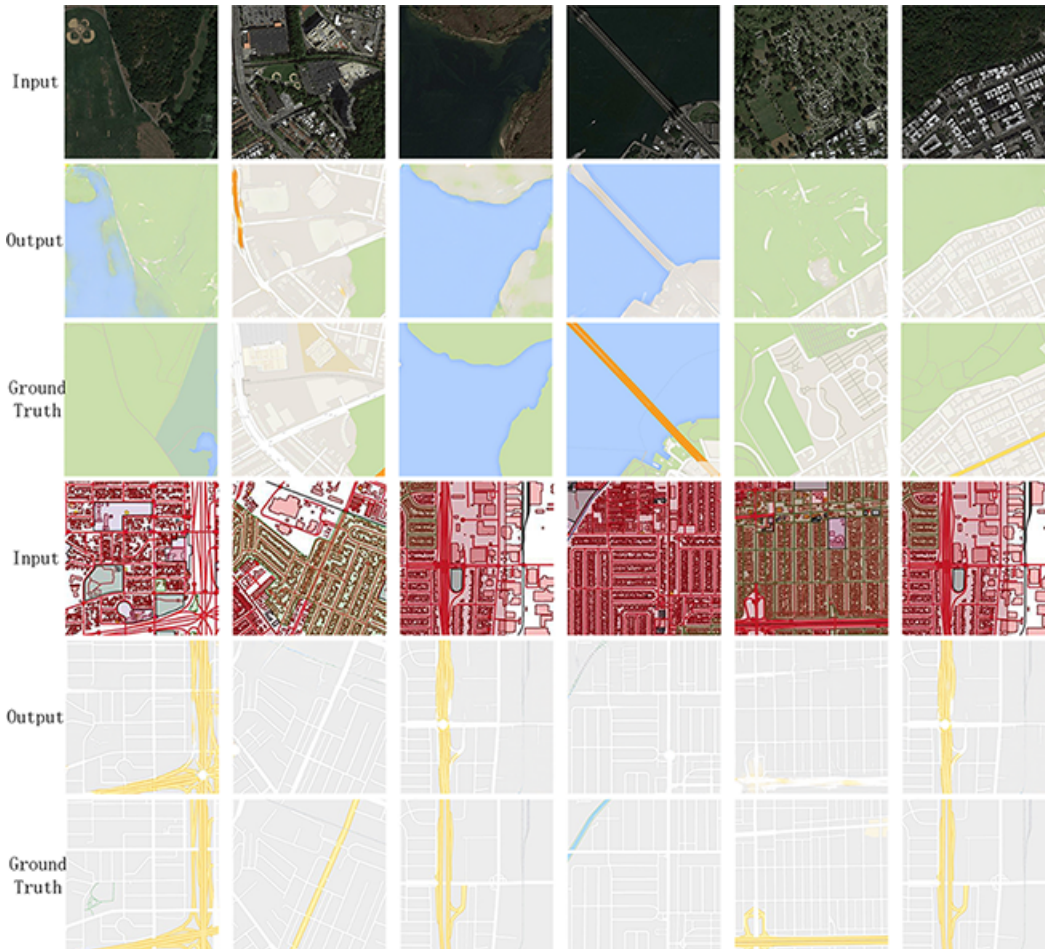


Figure 11: Typical remained errors.

According to the performance comparison among the baselines and our  $S^2OMGAN$  model, ours outperforms the SOTA baselines under objective and subjective metrics. Online maps generated by  $S^2OMGAN$  have higher MSE, SSIM, and ESSI score and win more human approval. However, flaws remain in maps generated by  $S^2OMGAN$ . We could see issues from Figure 11, such as confusing water and plants, hardly distinguishing objects covered by shade. Besides, some incorrect topological relations and irregular object shapes still exist due to a lack of corresponding information from the input image.

## 5 Conclusion

In this work, we put forward a novel semi-supervised structure augmented model,  $S^2OMGAN$  to automatically generate online maps. This strategy which is pre-trained with unpaired data and fine-trained with paired data shows the potential to generate more real online maps with lesser paired samples. We also show that topological consistency is very important to improve the fidelity of generated online maps. The designed image gradient L1 loss (GraL1) and image gradient structure loss (GraStr) are simple but effective loss functions to capture the topological consistency of generated online maps. Moreover, a new full-reference metric, ESSI, which focuses on topological relationship quality of objects of the generated map is proposed to assess topological consistency between generated maps and their ground truths. The Experiments show that  $S^2OMGAN$  outperforms the SOTA baselines in objective metrics and subjective human perceptual evaluation, which shows

the effectiveness of our model. In future works, we will focus on erroneous objects translation, wrong topological relations and shade problems in generated maps.

## Acknowledgment

The authors would like to thank the funding and support from the Advance Research Projects of Civil Aerospace Technology, Intelligent Distribution Technology of Domestic Satellite Information, No. B0301, and the National Science Foundation of China (grant numbers 41871364, 41571397, 41871276, and 51678077). Thanks for Shazonn and those inspiring S. Chen to be a determined hard worker. Thanks to T. Xu's granny Ms. Mengjun Yan, R.I.P.

## References

- [1] P. Haunold and W. Kuhn, "A keystroke level analysis of manual map digitizing," in *Spatial Information Theory A Theoretical Basis for GIS*, ser. Lecture Notes in Computer Science, A. U. Frank and I. Campari, Eds. Springer Berlin Heidelberg, 1993, pp. 406–420.
- [2] Y. Kang, S. Gao, and R. E. Roth, "Transferring Multiscale Map Styles Using Generative Adversarial Networks," *International Journal of Cartography*, vol. 5, no. 2-3, pp. 115–141, May 2019, arXiv: 1905.02200. [Online]. Available: <http://arxiv.org/abs/1905.02200>
- [3] F. Han, H. Zhang, S. Chatterjee, Q. Guo, and S. Wan, "A Modified Generative Adversarial Nets Integrated With Stochastic Approach for Realizing Super-Resolution Reservoir Simulation," *IEEE Transactions on Geoscience and Remote Sensing*, pp. 1–12, 2019.
- [4] K. Jiang, Z. Wang, P. Yi, G. Wang, T. Lu, and J. Jiang, "Edge-Enhanced GAN for Remote Sensing Image Superresolution," *IEEE Transactions on Geoscience and Remote Sensing*, vol. 57, no. 8, pp. 5799–5812, Aug. 2019.
- [5] J. M. Haut, R. Fernandez-Beltran, M. E. Paoletti, J. Plaza, A. Plaza, and F. Pla, "A New Deep Generative Network for Unsupervised Remote Sensing Single-Image Super-Resolution," *IEEE Transactions on Geoscience and Remote Sensing*, vol. 56, no. 11, pp. 6792–6810, Nov. 2018.
- [6] X. Wang, H. Yan, C. Huo, J. Yu, and C. Pant, "Enhancing Pix2pix for Remote Sensing Image Classification," in *2018 24th International Conference on Pattern Recognition (ICPR)*, Aug. 2018, pp. 2332–2336, iSSN: 1051-4651.
- [7] L. Zhu, Y. Chen, P. Ghamisi, and J. A. Benediktsson, "Generative Adversarial Networks for Hyperspectral Image Classification," *IEEE Transactions on Geoscience and Remote Sensing*, vol. 56, no. 9, pp. 5046–5063, Sep. 2018.
- [8] X. Wang, K. Tan, Q. Du, Y. Chen, and P. Du, "Caps-TripleGAN: GAN-Assisted CapsNet for Hyperspectral Image Classification," *IEEE Transactions on Geoscience and Remote Sensing*, vol. 57, no. 9, pp. 7232–7245, Sep. 2019.
- [9] M. Uricar, P. Krizek, D. Hurych, I. Sobh, S. Yogamani, and P. Denny, "Yes, we GAN: Applying Adversarial Techniques for Autonomous Driving," *arXiv:1902.03442 [cs]*, Feb. 2019, arXiv: 1902.03442. [Online]. Available: <http://arxiv.org/abs/1902.03442>
- [10] M. Frid-Adar, E. Klang, M. Amitai, J. Goldberger, and H. Greenspan, "Synthetic data augmentation using GAN for improved liver lesion classification," in *2018 IEEE 15th International Symposium on Biomedical Imaging (ISBI 2018)*, Apr. 2018, pp. 289–293.
- [11] M. Zhang, M. Gong, Y. Mao, J. Li, and Y. Wu, "Unsupervised Feature Extraction in Hyperspectral Images Based on Wasserstein Generative Adversarial Network," *IEEE Transactions on Geoscience and Remote Sensing*, vol. 57, no. 5, pp. 2669–2688, May 2019.
- [12] H. Wu, S. Zheng, J. Zhang, and K. Huang, "GP-GAN: Towards Realistic High-Resolution Image Blending," in *Proceedings of the 27th ACM International Conference on Multimedia*, ser. MM '19. New York, NY, USA: ACM, 2019, pp. 2487–2495, event-place: Nice, France. [Online]. Available: <http://doi.acm.org/10.1145/3343031.3350944>

- [13] A. T. Tran, T. Hassner, I. Masi, E. Paz, Y. Nirkin, and G. Medioni, “Extreme 3d Face Reconstruction: Seeing Through Occlusions,” in *2018 IEEE/CVF Conference on Computer Vision and Pattern Recognition*. Salt Lake City, UT: IEEE, Jun. 2018, pp. 3935–3944. [Online]. Available: <https://ieeexplore.ieee.org/document/8578512/>
- [14] M. Zhang, Y. Zhang, L. Zhang, C. Liu, and S. Khurshid, “DeepRoad: GAN-based Metamorphic Testing and Input Validation Framework for Autonomous Driving Systems,” in *Proceedings of the 33rd ACM/IEEE International Conference on Automated Software Engineering*, ser. ASE 2018. New York, NY, USA: ACM, 2018, pp. 132–142, event-place: Montpellier, France. [Online]. Available: <http://doi.acm.org/10.1145/3238147.3238187>
- [15] P. L. Suarez, A. D. Sappa, B. X. Vintimilla, and R. I. Hammoud, “Deep Learning Based Single Image Dehazing,” in *2018 IEEE/CVF Conference on Computer Vision and Pattern Recognition Workshops (CVPRW)*. Salt Lake City, UT, USA: IEEE, Jun. 2018, pp. 1250–12507. [Online]. Available: <https://ieeexplore.ieee.org/document/8575317/>
- [16] P. Isola, J.-Y. Zhu, T. Zhou, and A. A. Efros, “Image-To-Image Translation With Conditional Adversarial Networks,” 2017, pp. 1125–1134. [Online]. Available: [http://openaccess.thecvf.com/content\\_cvpr\\_2017/html/Isola\\_Image-To-Image\\_Translation\\_With\\_CVPR\\_2017\\_paper.html](http://openaccess.thecvf.com/content_cvpr_2017/html/Isola_Image-To-Image_Translation_With_CVPR_2017_paper.html)
- [17] J.-Y. Zhu, T. Park, P. Isola, and A. A. Efros, “Unpaired Image-To-Image Translation Using Cycle-Consistent Adversarial Networks,” 2017, pp. 2223–2232. [Online]. Available: [http://openaccess.thecvf.com/content\\_iccv\\_2017/html/Zhu\\_Unpaired\\_Image-To-Image\\_Translation\\_ICCV\\_2017\\_paper.html](http://openaccess.thecvf.com/content_iccv_2017/html/Zhu_Unpaired_Image-To-Image_Translation_ICCV_2017_paper.html)
- [18] M.-Y. Liu, T. Breuel, and J. Kautz, “Unsupervised Image-to-Image Translation Networks,” in *Advances in Neural Information Processing Systems 30*, I. Guyon, U. V. Luxburg, S. Bengio, H. Wallach, R. Fergus, S. Vishwanathan, and R. Garnett, Eds. Curran Associates, Inc., 2017, pp. 700–708. [Online]. Available: <http://papers.nips.cc/paper/6672-unsupervised-image-to-image-translation-networks.pdf>
- [19] Y. Alami Mejjati, C. Richardt, J. Tompkin, D. Cosker, and K. I. Kim, “Unsupervised Attention-guided Image-to-Image Translation,” in *Advances in Neural Information Processing Systems 31*, S. Bengio, H. Wallach, H. Larochelle, K. Grauman, N. Cesa-Bianchi, and R. Garnett, Eds. Curran Associates, Inc., 2018, pp. 3693–3703. [Online]. Available: <http://papers.nips.cc/paper/7627-unsupervised-attention-guided-image-to-image-translation.pdf>
- [20] S. Ganguli, P. Garzon, and N. Glaser, “GeoGAN: A Conditional GAN with Reconstruction and Style Loss to Generate Standard Layer of Maps from Satellite Images,” *arXiv:1902.05611 [cs]*, Feb. 2019, arXiv: 1902.05611. [Online]. Available: <http://arxiv.org/abs/1902.05611>
- [21] U. Demir and G. Unal, “Patch-Based Image Inpainting with Generative Adversarial Networks,” *arXiv:1803.07422 [cs]*, Mar. 2018, arXiv: 1803.07422. [Online]. Available: <http://arxiv.org/abs/1803.07422>
- [22] J. Neumann, “The Topological Information Content of a Map / An Attempt At A Rehabilitation Of Information Theory In Cartography,” *Cartographica: The International Journal for Geographic Information and Geovisualization*, 1994. [Online]. Available: <https://www.utpjournals.press/doi/abs/10.3138/U626-551H-64K4-9687>
- [23] T. Salimans, I. Goodfellow, W. Zaremba, V. Cheung, A. Radford, X. Chen, and X. Chen, “Improved Techniques for Training GANs,” in *Advances in Neural Information Processing Systems 29*, D. D. Lee, M. Sugiyama, U. V. Luxburg, I. Guyon, and R. Garnett, Eds. Curran Associates, Inc., 2016, pp. 2234–2242. [Online]. Available: <http://papers.nips.cc/paper/6125-improved-techniques-for-training-gans.pdf>
- [24] M. Heusel, H. Ramsauer, T. Unterthiner, B. Nessler, and S. Hochreiter, “GANs Trained by a Two Time-Scale Update Rule Converge to a Local Nash Equilibrium,” in *Advances in Neural Information Processing Systems 30*, I. Guyon, U. V. Luxburg, S. Bengio, H. Wallach, R. Fergus, S. Vishwanathan, and R. Garnett, Eds. Curran Associates, Inc., 2017, pp. 6626–6637.
- [25] M. Mirza and S. Osindero, “Conditional Generative Adversarial Nets,” *arXiv:1411.1784 [cs, stat]*, Nov. 2014, arXiv: 1411.1784. [Online]. Available: <http://arxiv.org/abs/1411.1784>

- [26] X. Huang, M.-Y. Liu, S. Belongie, and J. Kautz, “Multimodal Un-supervised Image-to-image Translation,” 2018, pp. 172–189. [Online]. Available: [http://openaccess.thecvf.com/content\\_ECCV\\_2018/html/Xun\\_Huang\\_Multimodal\\_Unsupervised\\_Image-to-image\\_ECCV\\_2018\\_paper.html](http://openaccess.thecvf.com/content_ECCV_2018/html/Xun_Huang_Multimodal_Unsupervised_Image-to-image_ECCV_2018_paper.html)
- [27] J.-Y. Zhu, R. Zhang, D. Pathak, T. Darrell, A. A. Efros, O. Wang, and E. Shechtman, “Toward Multimodal Image-to-Image Translation,” in *Advances in Neural Information Processing Systems 30*, I. Guyon, U. V. Luxburg, S. Bengio, H. Wallach, R. Fergus, S. Vishwanathan, and R. Garnett, Eds. Curran Associates, Inc., 2017, pp. 465–476. [Online]. Available: <http://papers.nips.cc/paper/6650-toward-multimodal-image-to-image-translation.pdf>
- [28] H. Zhang, T. Xu, and H. Li, “StackGAN: Text to Photo-Realistic Image Synthesis with Stacked Generative Adversarial Networks,” in *2017 IEEE International Conference on Computer Vision (ICCV)*. Venice: IEEE, Oct. 2017, pp. 5908–5916. [Online]. Available: <http://ieeexplore.ieee.org/document/8237891/>
- [29] Y. Choi, M. Choi, M. Kim, J.-W. Ha, S. Kim, and J. Choo, “StarGAN: Unified Generative Adversarial Networks for Multi-Domain Image-to-Image Translation,” 2018, pp. 8789–8797. [Online]. Available: [http://openaccess.thecvf.com/content\\_cvpr\\_2018/html/Choi\\_StarGAN\\_Unified\\_Generative\\_CVPR\\_2018\\_paper.html](http://openaccess.thecvf.com/content_cvpr_2018/html/Choi_StarGAN_Unified_Generative_CVPR_2018_paper.html)
- [30] A. Almahairi, S. Rajeshwar, A. Sordoni, P. Bachman, and A. Courville, “Augmented CycleGAN: Learning Many-to-Many Mappings from Unpaired Data,” in *International Conference on Machine Learning*, Jul. 2018, pp. 195–204. [Online]. Available: <http://proceedings.mlr.press/v80/almahairi18a.html>
- [31] H. You, Y. Cheng, T. Cheng, C. Li, and P. Zhou, “Bayesian CycleGAN via Marginalizing Latent Sampling,” *arXiv:1811.07465 [cs, stat]*, Dec. 2018, arXiv: 1811.07465. [Online]. Available: <http://arxiv.org/abs/1811.07465>
- [32] M. Januszewski and V. Jain, “Segmentation-Enhanced CycleGAN,” *bioRxiv*, p. 548081, Feb. 2019. [Online]. Available: <https://www.biorxiv.org/content/10.1101/548081v1>
- [33] D. Engin, A. Genc, and H. Kemal Ekenel, “Cycle-Dehaze: Enhanced CycleGAN for Single Image Dehazing,” 2018, pp. 825–833. [Online]. Available: [http://openaccess.thecvf.com/content\\_cvpr\\_2018\\_workshops/w13/html/Engin\\_Cycle-Dehaze\\_Enhanced\\_CycleGAN\\_CVPR\\_2018\\_paper.html](http://openaccess.thecvf.com/content_cvpr_2018_workshops/w13/html/Engin_Cycle-Dehaze_Enhanced_CycleGAN_CVPR_2018_paper.html)
- [34] G. Lu, Z. Zhou, Y. Song, K. Ren, and Y. Yu, “Guiding the One-to-One Mapping in CycleGAN via Optimal Transport,” *Proceedings of the AAAI Conference on Artificial Intelligence*, vol. 33, no. 01, pp. 4432–4439, Jul. 2019. [Online]. Available: <https://www.aaai.org/ojs/index.php/AAAI/article/view/4355>
- [35] A. Baraldi, L. Bruzzone, and P. Blonda, “Quality assessment of classification and cluster maps without ground truth knowledge,” *IEEE Transactions on Geoscience and Remote Sensing*, vol. 43, no. 4, pp. 857–873, Apr. 2005. [Online]. Available: <http://ieeexplore.ieee.org/document/1411992/>
- [36] C. Sammut and G. I. Webb, *Encyclopedia of Machine Learning*. Springer Science & Business Media, Mar. 2011, google-Books-ID: i8hQhp1a62UC.
- [37] Z. Wang, A. C. Bovik, H. R. Sheikh, and E. P. Simoncelli, “Image Quality Assessment: From Error Measurement to Structural Similarity,” *IEEE TRANSACTIONS ON IMAGE PROCESSING*, vol. 13, no. 1, p. 15, 2004.
- [38] W. Xue, L. Zhang, X. Mou, and A. C. Bovik, “Gradient Magnitude Similarity Deviation: A Highly Efficient Perceptual Image Quality Index,” *IEEE Transactions on Image Processing*, vol. 23, no. 2, pp. 684–695, Feb. 2014.
- [39] L. Ding, H. Huang, and Y. Zang, “Image Quality Assessment Using Directional Anisotropy Structure Measurement,” *IEEE Transactions on Image Processing*, vol. 26, no. 4, pp. 1799–1809, Apr. 2017.

- [40] Y. Taigman, A. Polyak, and L. Wolf, “Unsupervised Cross-Domain Image Generation,” *arXiv:1611.02200 [cs]*, Nov. 2016, arXiv: 1611.02200. [Online]. Available: <http://arxiv.org/abs/1611.02200>
- [41] J. Canny, “A Computational Approach to Edge Detection,” *IEEE Transactions on Pattern Analysis and Machine Intelligence*, vol. PAMI-8, no. 6, pp. 679–698, Nov. 1986.
- [42] K. He, X. Zhang, S. Ren, and J. Sun, “Deep Residual Learning for Image Recognition,” 2016, pp. 770–778. [Online]. Available: [http://openaccess.thecvf.com/content\\_cvpr\\_2016/html/He\\_Deep\\_Residual\\_Learning\\_CVPR\\_2016\\_paper.html](http://openaccess.thecvf.com/content_cvpr_2016/html/He_Deep_Residual_Learning_CVPR_2016_paper.html)
- [43] C. Chu, A. Zhmoginov, and M. Sandler, “CycleGAN, a Master of Steganography,” *arXiv:1712.02950 [cs, stat]*, Dec. 2017, arXiv: 1712.02950. [Online]. Available: <http://arxiv.org/abs/1712.02950>
- [44] M. Pecka, K. Zimmermann, M. Petrлік, and T. Svoboda, “Data-Driven Policy Transfer With Imprecise Perception Simulation,” *IEEE Robotics and Automation Letters*, vol. 3, no. 4, pp. 3916–3921, Oct. 2018.